Separation and Purification Technology 211 (2019) 768–781

Contents lists available at ScienceDirect

Separation and Purification Technology

journal homepage: www.elsevier.com/locate/seppur

Filterability prediction of needle-like crystals based on particle size and shape distribution data

Giulio Perini[a], Fabio Salvatori[b], David R. Ochsenbein[b,1], Marco Mazzotti[b], Thomas Vetter[a,*]

[a] University of Manchester, School of Chemical Engineering and Analytical Science, M13 9PL Manchester, United Kingdom
[b] ETH Zurich, Institute of Process Engineering, Sonneggstrasse 3, CH-8092 Zurich, Switzerland

ARTICLE INFO

Keywords:
Filtration
Needle-like crystals
Particle size and shape

ABSTRACT

The isolation and further treatment of particles generated in a crystallization process is dependent on their size and shape. The work presented here analyzes the filtration performance of needle-like particles, which often exhibit long filtration times or high retention of mother liquor. The size and shape of populations of β L-Glutamic Acid and γ D-Mannitol particles are measured using an automated image analysis approach (as well as a standard light scattering method), and their associated cake resistance is determined in pressure filtration experiments. Using a partial least squares regression analysis we develop a model of the process and show that relative cake resistances can be predicted if the particle size distributions are accurately known. Furthermore, we show that the statistical model calibrated on a single compound (either of those used for this study), can be exploited to predict the relative cake resistances of another compound.

1. Introduction

The fine chemical and pharmaceutical industries make extensive use of crystallization in the production of chemicals and active compounds, due to its ability to produce highly pure substances. The crystallization step is typically embedded into a chain of unit operations. It is a crucial step, as its operating conditions significantly affect properties of the powder, which in turn affect the downstream process operations (filtration/centrifugation, washing, drying, etc.) [1]. Filtration in particular, commonly performed right after crystallization to physically separate the formed crystals from the mother liquor, is strongly influenced by the outcome of crystallization; specifically by the size and shape of the crystals [2].

Filtration can be described as the flow of a liquid through a porous medium driven by a gradient in pressure. In the case of filtration of crystals, the liquid is the mother liquor that needs to be recovered or separated from the crystalline products and the porous bed consists of the filter medium as well as the solids accumulating on top of it in the form of a filter cake. The permeability of the latter plays the most significant role in determining the performance of a filtration process, as its resistance tends to dominate. However, forecasting cake resistance has proven difficult due to the aforementioned effect of particle geometry: size and shape determine the way particles stack and therefore the cake's porous structure. Alas, the particle size and shape distribution (PSSD) is in itself hard to measure and the quantitative relationship between it and cake permeability is not known.

The qualitative influence of the shape of crystals on filterability on the other hand has been known for a long time and has been investigated multiple times [3]. Literature proffers general statements of the impact of shape [4], as well as compound specific correlations [5–7]. Knowledge is also available on how to predict filterability via modeling [8]. The modeling approaches, however, employ theories, such as the Carman-Kozeny equation, that are based on strong assumptions; in particular they assume monodisperse spherical particles [9,10]. In order to adequately describe the filtration behavior in the case of non-equant particles, it would be valuable to be able to quantitatively model the effect of both size and shape on the structure of a filter cake. In this context, the work of Bourcier et al. [11] represents an important step towards the characterization of how anisotropic particles behave during filtration; it describes how the cake resistance of differently shaped particles of the same substance can be accurately modeled if knowledge of physical data of the model substance, particle size and shape data, as well as characteristic values of the filter cake formed, namely its porosity and tortuosity, are known. Since there are, as of now, no general approaches to predict the cake porosity and tortuosity of a filter cake consisting of non-equant particles of different sizes, the extension of Bourcier et al.'s approach to particles other than those characterized experimentally is difficult. However, if this gap

* Corresponding author.
E-mail address: thomas.vetter@manchester.ac.uk (T. Vetter).
[1] Present address: Janssen: Pharmaceutical Companies of Johnson & Johnson, Hochstrasse 201, CH-8200 Schaffhausen, Switzerland.

https://doi.org/10.1016/j.seppur.2018.10.042
Received 3 May 2018; Received in revised form 16 September 2018; Accepted 17 October 2018
Available online 19 October 2018

Notation

Symbols

A_f	effective filtration area [m^2]
A_c	funnel (and cake) cross-sectional area [m^2]
d	quantile of PSD [m]
e	efficiency (statistical parameter) [–]
k	kurtosis of particle length [–]
L	particle length [m]
m_c	cake mass [kg]
m	filtrate mass [kg]
P	pressure [Pa]
R	cooling rate $\left[\frac{°C}{h}\right]$
s	skewness of particle length [–]
t	time [s]
T	temperature [°C]
V	filtrate volume [m^3]
$\dot{V}$	volumetric flow rate $\left[\frac{m^3}{s}\right]$

Greek letters

α	cake resistance $\left[\frac{m}{kg}\right]$
$\widetilde{\alpha}$	relative cake resistance [–]
β	medium resistance $\left[\frac{1}{m}\right]$
δ	convergence criterion [–]
η	dynamic viscosity [Pa s]
λ	slope of filtration profiles $\left[\frac{kg}{s}\right]$
ρ_l	density of solution $\left[\frac{kg}{m^3}\right]$
σ	standard deviation of particle length [m]
τ	Kendall's ranking coefficient [–]
Φ	aspect ratio [–]
χ	sieve mesh [m]
ω	rotational speed [rpm]

Acronyms

FTC	flow through cell
LD	laser diffraction
LGA	β L-Glutamic Acid
LV	latent variable
MAE	mean absolute error
MAN	γ D-Mannitol
MSG	monosodium glutamate hydrate
PLS	partial least squares
PSD	particle size distribution
PSSD	particle size and shape distribution
VIP	variable importance in projection

were successfully closed, more efficient filtration operations could be designed by relying on the extensive knowledge available on tuning the size and shape of particles generated from a crystallization process [12–15].

Hitherto, the study of non-spherical particles was hindered by the lack of measurement devices that allow for fast and statistically significant measurements of PSSDs. However, the advancements of imaging and computational techniques [16–19] have now made the robust measurement of PSSDs feasible.

The present work aims at exploiting these novel technologies to determine the quantitative link between crystallization and filtration for non-isotropic particles. In particular, needle-like crystals have been investigated, as they are ubiquitous and obviously deviate strongly from spheres. We report experimental data regarding cake resistances for powders that have been pre-treated in different ways, resulting in a diverse set of particle size and shape distributions. The techniques employed here, such as milling [20] and temperature cycling [15,21–23], are widely used in practice to improve the processability of crystals. In order to decouple the effect of other properties that might influence filterability, experiments have been performed with two systems of similar macroscopic shape, but different chemical nature; these are, β L-Glutamic Acid and γ D-Mannitol. Powders have then been characterized with a custom-built stereoscopic imaging device [16] and with a commercially available laser diffraction (LD) instrument. The former yields particle size and shape distributions, while the latter provides only particle size data. The specific cake resistance of the different powders was characterized through percolation experiments performed on consolidated cakes. We present a regression model to link the PSSDs or PSDs with the cake resistances of each compound and analyze whether having access to particle size and shape data is beneficial in comparison to size data only. Unlike previous works [6,24], which generated compound-specific models that are not readily portable to other compounds, we attempt to calibrate the regression model using data from one compound and to apply it to a different compound with similar macroscopic shape.

This work is organized as follows: first, the experimental methods and techniques are presented in Section 2. Here, the theory used for filtration characterization is also presented along with the regression analysis method used. The results obtained from filtration experiments and regression analysis are presented, analyzed and discussed in Section 3, while in Section 4 conclusions are drawn.

2. Materials and methods

The particle size and shape distribution of crystals, as well as a measure of filterability of crystals of two different compounds, were experimentally investigated. Powders of β L-Glutamic Acid (LGA) and γ D-Mannitol (MAN) crystals were first crystallized and then treated in order to generate populations that exhibit a wide variety of PSSDs.

2.1. Materials

2.1.1. β L-Glutamic Acid

The production of β L-Glutamic Acid crystals has been performed via pH-shift as described in Ochsenbein et al. [25]. Briefly re-stated, monosodium glutamate hydrate (MSG; Sigma Aldrich, Buchs, Switzerland, purity ⩾98%) and hydrochloric acid (HCl, Sigma Aldrich, Buchs, Switzerland, fuming ⩾37%) were used as delivered. Deionized and filtered (filter size 0.22 μm) water was obtained from a Milli-Q Advantage A10 system (Millipore, Zug, Switzerland). LGA crystallizes in two known polymorphs, namely the metastable α and the stable β polymorph, which are monotropically related. The production of crystals was performed in two steps: first, equimolar amounts of MSG and HCl were mixed in water under continuous stirring for one hour at 5 °C; during this step, α LGA crystals were formed. Subsequently, these crystals were fed into a saturated solution (w.r.t. the α form) at 45 °C, created by mixing equimolar amounts of MSG and HCl; the crystals were then allowed to transform to the β polymorph over a period of 15 h, after which they were filtered in a Büchner funnel and eventually dried in an oven without agitation.

2.1.2. γ D-Mannitol

The production of γ D-Mannitol crystals has been performed via seeded cooling crystallization. MAN (Sigma Aldrich, Buchs,

Switzerland, purity ⩾98%) was used as delivered to generate saturated solutions and for the production of seeds. Deionized and filtered water (as before) was used in combination with 2-propanol (Sigma Aldrich, Buchs, Switzerland, purity ⩾99.5%) as solvent. Crystals were prepared by putting seeds of γ D-Mannitol (the stable polymorph) in a saturated solution (90 wt% water and 10 wt% 2-propanol) of MAN at 30 °C in a 10 L stirred reactor. The suspension was then cooled to 5 °C in 16.7 h and kept at constant conditions for 15 h before it was filtered. The cake was then washed with 2-propanol in order to remove the trapped mother liquor and prevent agglomeration; finally the powder was dried in an oven without agitation.

2.2. Preparation and characterization of crystals

A fraction of the crystals produced above was used as is (population 1). The rest was further treated to alter the size and shape distributions. The techniques used to achieve this goal are milling, sieving and a combination of milling and temperature cycles. The methodologies used are summarized here and the exact conditions are reported in Table 1. After each of these steps particles were isolated by filtration, washed (in the case of MAN) and dried (as above).

2.2.1. Wet milling

Wet milling is a size-reduction technology extensively used in industry to obtain smaller crystals [26,27]. This technique was exploited to break needle-like particles to obtain a population of crystals with lower aspect ratio and smaller size compared to the base case (population 1, see above). Wet milling was performed with a rotor-stator mill (MK module, magic LAB, IKA - Werke, Germany) operated at a defined rotation speed ω (see Table 1) coupled with a thermostat (Ministat 230 with Pilot ONE, Huber Kältemaschinenbau, Germany) to keep the temperature of the mill at 20 °C. The resulting particle population is termed population 2.

2.2.2. Temperature cycles

A fraction of population 2 was further treated with temperature cycles. Temperature cycles exploit the temperature dependency of the solubility of the compound in the selected solvent to perform dissolution at high temperature followed by recrystallization at low temperature [21,28–30]. Each cycle results in the dissolution of the smallest particles followed by the growth of the surviving ones. The extent of the resulting increase in average size can be tuned by varying the number of cycles, as well as their temperature high and low points [15,31]. Here, a single temperature cycle has been performed after milling of the crystals (see above). Initial temperature (T_{start}), maximum temperature (T_{max}) and final temperature (T_{end}), as well as cooling rate (R), are given in Table 1 for both compounds. The resulting particle population is termed population 3.

2.2.3. Dry sieving

A fraction of population 1 has been dry-sieved in order to generate populations of crystals with similar shapes but different average sizes. Analytical sieves (Fritsch, Idar-Oberstein, Germany) have been used for this purpose, with mesh sizes as specified by the parameter χ in Table 1. The resulting particle populations are referred to as population 4A and 4B.

It is important to highlight that, for non-isotropic crystals, such as needles, we do not expect a sharp cut between the population above and the one below the sieve. This is due to the fact that the chance of a specific needle-like particle to cross the sieve mesh significantly depends on its orientation with respect to the sieve.

2.2.4. Characterization – size distribution measurement using laser diffraction

The 1D particle size distribution (PSD) of crystals was measured using laser diffraction (LD). Measurements were performed with a Malvern Mastersizer 2000. The crystals were suspended in a saturated solution and then circulated inside the equipment. For each population three samples were measured in order to check repeatability. The software provided with the Malvern Mastersizer converts the measured scattering pattern into a 1D PSD implicitly assuming spherical particles. Therefore, there is an inherent error in the 1D PSDs when non-isotropic particles are measured [32–35].

2.2.5. Characterization – particle size and shape distribution measurement by imaging

The determination of the two-dimensional particle size and shape distributions of the produced populations has been performed using an ex situ, stereoscopic imaging apparatus, referred to as the flow through cell (FTC) [16,36]; its schematic representation is shown in Fig. 1. Briefly described, particles flowing through a sapphire glass cell are photographed from two orthogonal directions multiple times per second. Using this procedure, two projections are obtained for each crystal measured, which in turn allows to reconstruct the three-dimensional shape of the measured particles. Through the acquisition of a large number of images, it is possible to gather a substantial quantity of information in a short time, allowing for a statistically significant measurement. In this work, the needle-like LGA and MAN particles were characterized as cylinders of height L_1 and diameter L_2.

2.3. Filtration

2.3.1. Experimental procedure

The filtration performance of the crystals generated above was characterized through pressure filtration experiments. The pressure filtration experiments were performed in a custom laboratory setup, shown schematically in Fig. 2. A stainless steel filtration funnel (Pall Corporation, Port Washington, United States), serving as a pocket filter, is equipped with a ball valve and a pressure transducer. A nitrogen

Table 1
Summary of experimental conditions to generate particle populations of LGA and MAN.

Compound	Pop. 1 Base Case	Pop. 2 Milled	Pop. 3 Milled + T-Cycle	Pop. 4 A Sieved Above	Pop. 4B Sieved Below
LGA					
Production	pH shift	pH shift	pH shift	pH shift	pH shift
Transformation	none	wet milling in water ω = 10, 000 rpm	wet milling in water ω = 10, 000 rpm, one T-Cycle, T_{start} = 33 °C, T_{max} = 42 °C, T_{end} = 25 °C, R = 3 °C h^{-1}	sieving χ = 180 μm frac.: above	sieving χ = 180 μm frac.: below
MAN					
Production	cooling crystallization	cooling crystallization	cooling crystallization	cooling crystallization	cooling crystallization
Transformation	none	wet milling in 2-propanol ω = 10, 000 rpm	wet milling in 2-propanol ω = 10, 000 rpm, one T-cycle, T_{start} = 30 °C, T_{max} = 35 °C, T_{end} = 25 °C, R = 3 °C h^{-1}	sieving χ = 450 μm frac.: above	sieving χ = 450 μm frac.: below

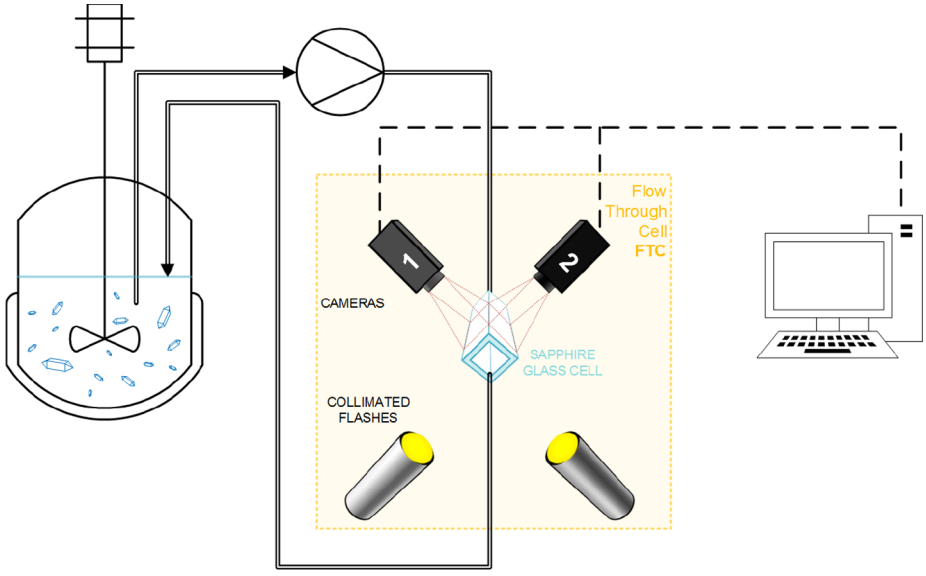

Fig. 1. Schematic depiction of stereoscopic flow cell [16,36] used for characterization of particle size and shape distributions.

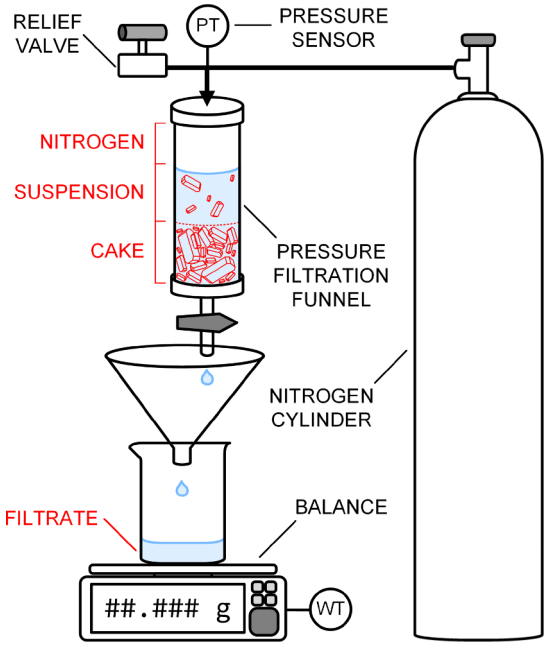

Fig. 2. Schematic representation of the pressure filtration plant.

cylinder equipped with a pressure regulator is used to bring the pressure inside the funnel to the desired level. A balance is used to record the filtrate mass over time. Details about the dimensions and the specifications of the pocket filter are given in the supplementary material.

In the initial step of each experiment a filter cake was formed. To this end, the filtration funnel was filled with a fixed amount of saturated solution and a defined mass of crystals (see Table 2). After pressurizing the system, filtration was initiated by opening the bottom valve. Once the level of suspension reached the top of the cake, the deliquoring phase started.[2] In this stage part of the liquid trapped in the cake left the system while part of it remained in the cake. When deliquoring approached the end, the bottom valve and the cylinder were closed and the residual pressure released through the relief valve. The solid lines shown in Fig. 3 (top) show the evolution of the filtrate mass collected on the balance over time during this cake formation step, while the evolution of the pressure is shown in the bottom subfigures. It is evident that the pressure drop over the cake is kept constant in the cake formation phase, but decreases during the deliquoring phase (only shown for LGA; left bottom panel).

Table 2
Summary of experimental conditions for pressure filtration.

	LGA	MAN
Pressures investigated	0.75 barg 1.50 barg 2.25 barg	0.75 barg 1.50 barg 2.25 barg
Deliquoring	Present	Absent
Solution	Saturated solution of LGA in Water	Saturated solution of MAN in 2-propanol
Crystal mass	20 g	20 g
Solution mass	150 g	varies

The filter cakes were subsequently subjected to multiple percolations. Percolations were performed by adding new batches of saturated solution on top of the filter cake, which where subsequently filtered using a constant pressure differential (see dashed lines in the bottom panels of Fig. 3). As can be seen from the dashed lines in the top panels of this Figure, the slope in the linear part of the filtrate mass vs. time profile decreases with each percolation (only first and last percolation shown), which is likely related to the compaction and compression of the filter cake. Percolations were performed until a stable cake structure was reached. In order to determine when this stable structure was reached, the slopes of the linear sections of the filtrate mass over time profiles, λ, were analyzed. A convergence parameter, δ, based on the variation of these slopes, was defined:

$$\delta_i = \left| \frac{\lambda_i - \lambda_{i-1}}{\lambda_{i-1}} \right| \quad i = 2, 3, \ldots \tag{1}$$

where i refers to the i-th percolation step. An experiment was considered successfully converged when three subsequent percolations with an absolute value of the parameter δ_i smaller than or equal to 5% were performed.

[2] Note that deliquoring was only performed for LGA samples, as deliquoring MAN filter cakes led to the formation of holes and cracks; a discussion of the effect of this difference in methodology is included in the supplementary material.

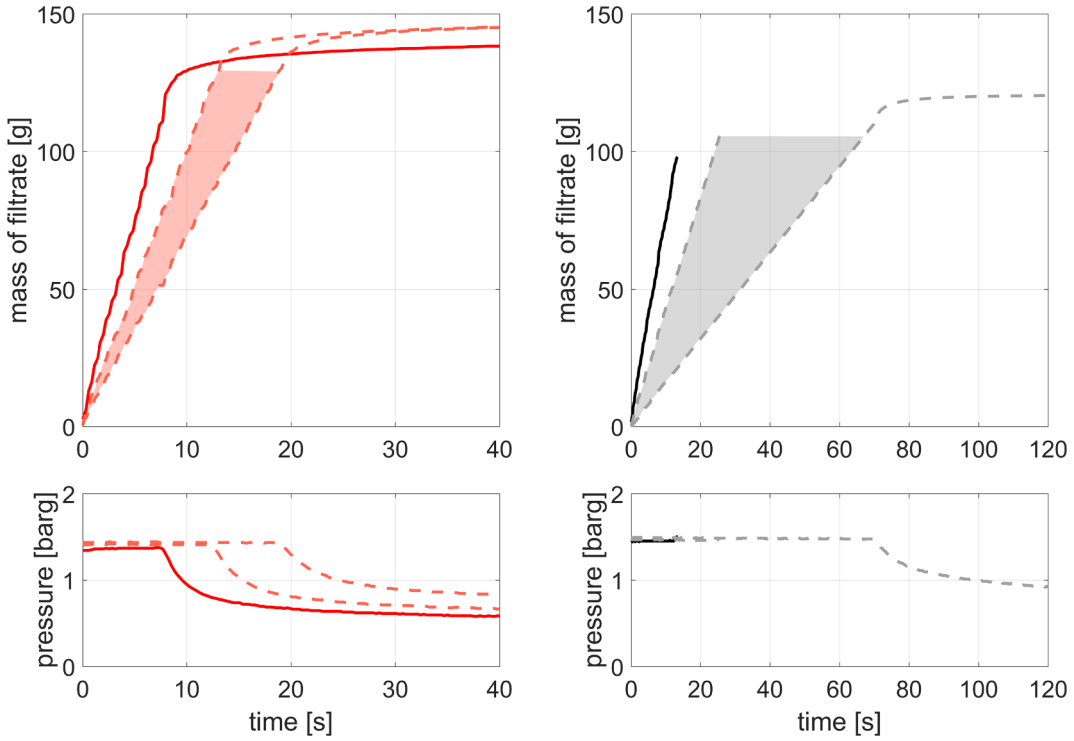

Fig. 3. Typical evolution of mass of filtrate and pressure in experiments with deliquoring phase (on the left, performed with LGA) and without deliquoring phase (on the right, performed with MAN). Solid lines indicate cake formation; dashed lines indicate first and last percolations. Colored areas indicate the range of profiles observed in percolations. Both examples have been performed with population 1 of each compound at 1.50 barg. In the case of MAN the cake only undergoes deliquoring during the last percolation.

2.3.2. Determination of average specific cake resistances for percolations performed on stable cake structures

In the remainder of this paper, we aim at relating the resistance that the filter cake and medium pose to the flow of filtrate to the particle size and shape distribution of the crystals in the filter cake. Specifically, we limit ourselves to analyzing the cases where stable cake structures have already been established (according to the convergence criterion mentioned in Eq. (1)). In such cases, the rate of filtrate leaving the filtration device can be described as the flow of a liquid through a porous medium (the filter cake) according to Darcy's law [37,38]:

$$\frac{\dot{V}}{A_f} = \frac{\Delta P}{\eta\left(\beta + \alpha\frac{m_c}{A_c}\right)} \tag{2}$$

This correlates the volumetric flow rate of filtrate, $\dot{V}$, per unit of effective filtration area, A_f, to the pressure drop across the cake, ΔP, the dynamic viscosity of the fluid, η, and the resistance that the medium and cake pose, β and $\alpha\frac{m_c}{A_c}$, respectively. The area of filtration, A_f, might differ from the cross section of the cake, A_c, as not all the base might be active filtration area. The resistance of the cake is expressed here using α, the average specific cake resistance and the cake mass, m_c. When describing the percolation of particle free liquid through a cake with a stable structure, the cake mass, m_c, and its height remain constant over time. Under such conditions and assuming that the flow rate of filtrate is constant, Eq. (2) can be rearranged to yield the following relationship between volume of filtrate and time:

$$\frac{\eta}{\Delta P A_f}\left(\beta + \alpha\frac{m_c}{A_c}\right)V = t \tag{3}$$

Expressing the volume of filtrate through its mass and density this equation can be rearranged to linearly correlate time and mass of filtrate, m:

$$m = \frac{\rho_l}{\frac{\eta}{\Delta P A_f}\left(\beta + \alpha\frac{m_c}{A_c}\right)}t = \lambda t \tag{4}$$

This describes the initial linear part of the filtrate mass vs. time profile of percolations, see Fig. 3. The evaluation of the slope, λ, from this profile can then be used to obtain cake and medium resistances:

$$\alpha = \left[\frac{1}{\lambda}\frac{\rho_l \Delta P A_f}{\eta} - \beta\right]\frac{A_c}{m_c} \tag{5}$$

The characterization of the filter medium resistance, β, was carried out in the absence of a filter cake as explained in the supplementary material.

The above procedure to determine average specific cake resistances is consistent with the experimental conditions of our percolation experiments. Note, however, that these measurements differ from industrial-scale filtration where a filter cake is formed by flowing a suspension towards a filter medium continuously, i.e., the mass of crystals in the filter cake increases over time. This implies a decreasing rate of filtrate flowing through the cake over time (rather than the constant flow rate in percolation experiments presented here, cf. Fig. 3). The determination of cake resistances from such filtrate mass vs. time profiles requires a different analysis than the one performed above (see, e.g., Teoh et al. [39] and Tien [40]).

2.4. Regression analysis of cake resistances

The correlation between particle properties and filtration behavior can be analyzed with the use of statistical tools. These methods can be calibrated on a specific set of experimental data thus enabling the prediction of the same properties for a new dataset. The validity of this approach to correlate particle size distribution data and average specific cake resistances has already been shown in the literature [6,24]. Here, a partial least squares (PLS) regression [41] is used to examine

the interdependence between PSD and PSSD and the average specific cake resistance, α. Specifically, to isolate compound and system specific effects, which are outside the scope of this work, we define a relative cake resistance, $\tilde{\alpha}_{i,P}$:

$$\tilde{\alpha}_{i,P} = \frac{\alpha_{i,P}}{\alpha_{3,P}} \tag{6}$$

where all cake resistances are scaled with the cake resistance of population 3 of the same compound at a given pressure. This population was selected since it exhibited the lowest cake resistance for all experimental conditions; in this way the relative cake resistance indicates how far each measurement is from the best case reported. In Eq. (6) the subscript P denotes the pressure drop over the filter cake and i is the population index. The regression analysis was exploited to understand the ability of different particle data, namely PSDs and PSSDs, to predict the specific cake resistance. Multiple descriptors for these distributions have been investigated. For PSDs a successful approach proved to be the use of volume-weighted quantiles. For PSSDs statistical parameters derived from the moments of the distribution were the best set of descriptors among those considered. We here proceed with an in depth investigation of these cases and their combination; details and results of other options are presented in the supplementary material. Three possible predictor sets have been formulated as follows:

- Case 1 – *PSSD statistics – {20 predictors}*
  Twenty statistical parameters describing the mean, variance, skewness, etc. have been calculated for each PSSD, as presented in Table 3.
- Case 2 – *PSD quantiles (d_5, d_{10}, …, d_{95}) – {19 predictors}*
  These were obtained from the PSDs resulting from LD measurements.
- Case 3 – *PSSD statistics + PSD quantiles – {39 predictors}*
  A combination of the predictors of case 1 and 2 has been used.

The complete list of variables used as predictors in each case is reported in Table 4.

The PLS regression was performed with a *MATLAB* routine based on the *plsregress* function which is part of the *Statistics and Machine Learning Toolbox* [42]. This function implements the SIMPLS algorithm [43], which was used with centered and standardized predictors. Part of the filterability data was used as calibration set, while the remaining data were used to test the predictive capabilities of the model. Various calibration strategies have been implemented and their outcomes are presented in Section 3.4. All of them use experimental data from one specific pressure value, i.e., 1.50 barg and one compound, so that the data of the remaining compound can be used as test data.

The number of latent variables in the PLS models was chosen based on a leave-one-out cross validation procedure. This resulted in the choice of two latent variables in all cases where three or more calibration points were used. The quantitative error metric used for training, calibration and testing is the mean absolute error, defined as:

Table 4
Summary of the variables used for each analyzed case of PLS regression. For the definition of the statistical parameters see Table 3.

Var. #	Case 1	Case 2	Case 3
1	$\bar{L}_1$	d_5	$\bar{L}_1$
2	$\bar{L}_2$	d_{10}	$\bar{L}_2$
3	$\bar{\Phi}$	d_{15}	$\bar{\Phi}$
4	σ_{11}^2	d_{20}	σ_{11}^2
5	σ_{11}	d_{25}	σ_{11}
6	e_{11}	d_{30}	e_{11}
7	σ_{22}^2	d_{35}	σ_{22}^2
8	σ_{22}	d_{40}	σ_{22}
9	e_{22}	d_{45}	e_{22}
10	σ_{12}^2	d_{50}	σ_{12}^2
11	e_{12}	d_{55}	e_{12}
12	s_{111}	d_{60}	s_{111}
13	s_{222}	d_{65}	s_{222}
14	s_{112}	d_{70}	s_{112}
15	s_{122}	d_{75}	s_{122}
16	k_{1111}	d_{80}	k_{1111}
17	k_{2222}	d_{85}	k_{2222}
18	k_{1112}	d_{90}	k_{1112}
19	k_{1222}	d_{95}	k_{1222}
20	k_{1122}	–	k_{1122}
21	–	–	d_5
22	–	–	d_{10}
23	–	–	d_{15}
24	–	–	d_{20}
25	–	–	d_{25}
26	–	–	d_{30}
27	–	–	d_{35}
28	–	–	d_{40}
29	–	–	d_{45}
30	–	–	d_{50}
31	–	–	d_{55}
32	–	–	d_{60}
33	–	–	d_{65}
34	–	–	d_{70}
35	–	–	d_{75}
36	–	–	d_{80}
37	–	–	d_{85}
38	–	–	d_{90}
39	–	–	d_{95}

Table 3
Summary of statistical quantities describing the PSSDs used for regression analysis.[a,b]

Quantity type	Definition	Description
means	$\bar{L}_x = \frac{1}{n}\sum_{i=1}^{n} L_{x,i}$	Average value of the characteristic length x
mean aspect ratio	$\bar{\Phi} = \frac{1}{n}\sum_{i=1}^{n} \frac{L_{1,i}}{L_{2,i}}$	Average value of the aspect ratio
(co)variances	$\sigma_{xy}^2 = \frac{1}{n}\sum_{i=1}^{n} (L_{x,i} - \bar{L}_x)(L_{y,i} - \bar{L}_y)$	Measure of the broadness of the distribution
standard deviations	$\sigma_{xy} = \sqrt{\frac{1}{n}\sum_{i=1}^{n} (L_{x,i} - \bar{L}_x)(L_{y,i} - \bar{L}_y)}$	Measure of the broadness of the distribution
(co)efficiency	$e_{xy} = \frac{\sigma_{xy}^2}{\bar{L}_x \bar{L}_y}$	Measure of the relative broadness of the distribution
(co)skewness	$s_{xyz} = \frac{1}{n}\frac{\sum_{i=1}^{n}(L_{x,i} - \bar{L}_x)(L_{y,i} - \bar{L}_y)(L_{z,i} - \bar{L}_z)}{\sigma_{xx}\sigma_{yy}\sigma_{zz}}$	Measure of the asymmetry of the distribution
(co)kurtosis	$k_{xyza} = \frac{1}{n}\frac{\sum_{i=1}^{n}(L_{x,i} - \bar{L}_x)(L_{y,i} - \bar{L}_y)(L_{z,i} - \bar{L}_z)(L_{a,i} - \bar{L}_a)}{\sigma_{xx}\sigma_{yy}\sigma_{zz}\sigma_{aa}}$	Measure of the relative importance of tails

[a] n is the total number of particles per sample.
[b] $x, y, z, a \in \{1, 2\}$.

$$MAE = \frac{1}{n}\sum_{i=1}^{n} |\tilde{\alpha}_{exp,i} - \tilde{\alpha}_{PLS,i}| \tag{7}$$

The influence that each predictor has on the fitting was investigated in terms of VIP (variable importance in projection) scores. This is a useful tool for variable selection and retrospective analysis. The following expression, proposed by Chong and Jun [44], is adopted here:

$$VIP_i = \sqrt{p \sum_{k=1}^{h} [SS(b_k \mathbf{t}_k)(\mathbf{w}_{ik}/||\mathbf{w}_k||^2)] \Big/ \sum_{k=1}^{h} SS(b_k \mathbf{t}_k)} \tag{8a}$$

$$SS(b_k \mathbf{t}_k) = b_k^2 \mathbf{t}_k^T \mathbf{t}_k \tag{8b}$$

where p is the number of predictors, h is the number of latent variables, $\mathbf{b}$ represents the regression coefficients of the scores of the predictors, $\mathbf{t}$ the predictors' scores and $\mathbf{w}$ represents the weights. Note that the quantities in bold represent vectors. With this definition, only variables with a score larger than 1 are considered important.

The prediction performance of the developed tool for all cases studied was further investigated using Kendall's τ coefficient [45]; a rank correlation coefficient. This coefficient checks for accordance between ranks:

$$\tau = \frac{(\text{number of concordant pairs}) - (\text{number of discordant pairs})}{n(n-1)/2} \tag{9}$$

where n is the number of objects in the ranking, i.e., in our case the number of filterabilities compared with each other (five). τ is -1, when the predicted and measured rankings are fully discordant, and it becomes 1 when the rankings are completely concordant. Intermediate values indicate different levels of accordance and in particular a coefficient equal to 0 means that there is the same number of concordant and discordant pairs.

3. Results

3.1. Characterization of crystals

One of the goals of the present paper is to assess whether predictions of specific cake resistances based on full PSSDs are superior to those based on 1D particle size distributions. To enable this comparison, characterization results from laser diffraction (1D PSD) and the imaging device (2D PSSD) are reported and compared with each other in this section.

3.1.1. PSD

All the produced populations, five per compound, were examined and the reproducibility of measurements was confirmed by analyzing three different samples of each population. We present in Fig. 4(a) an overview of the PSDs obtained for both compounds, displaying LGA in red and MAN in gray. We can observe the following characteristics: first, the presence of a substantial fraction of fines is detected in all samples. Aligned with the production methods used, the highest quantity of fines is observed for populations 2 and 4B, where the crystals underwent milling and dry sieving, respectively. The particle populations that were treated with one temperature cycle, namely populations 3, feature the smallest amount of fines instead. Second, the populations of MAN generally include more fines than the corresponding samples of LGA.

3.1.2. PSSD

The flow through cell was used to determine the PSSDs for all populations of both compounds. Analogously to the PSD case, three samples of each population have been analyzed to check for reproducibility (see supplementary material). While each sample alone contains a statistically significant number of particles, we have combined the three samples, to obtain smooth PSSDs for all populations, as shown in Fig. 5. In the figure the volume-weighted PSSDs are shown using contours, which are isolines drawn at specific heights of the distribution.

The results indicate that, depending on the production method, populations with distinctly different PSSDs were obtained for each compound and, at the same time, populations of the two different compounds with comparable features were produced. Going in more detail for each compound, one sees that the samples prepared through the application of milling (population 2) exhibit the smallest crystals and a smaller aspect ratio compared to the other populations. This can be explained due to the fact that breaking a needle usually results in the formation of two smaller needles with the same diameter (L_2), but with a shorter length (L_1). Population 3 was produced from population 2 by adding a single temperature cycle. The larger particles observed in the corresponding PSSD and the absence of fines indicate that this procedure was successful in tuning the PSSD, as reported elsewhere [15,21,30,31].

3.1.3. Comparison of PSDs and PSSDs

To enable a direct comparison between PSD and PSSD measurements, the volume of each cylindrical particle detected in the FTC was determined and the diameter of the volume-equivalent sphere was calculated from it. The distribution of these volume-equivalent sphere diameters is reported in Fig. 4(b). Comparing the distributions in Fig. 4(a) and (b) we can see that there are several major differences: the

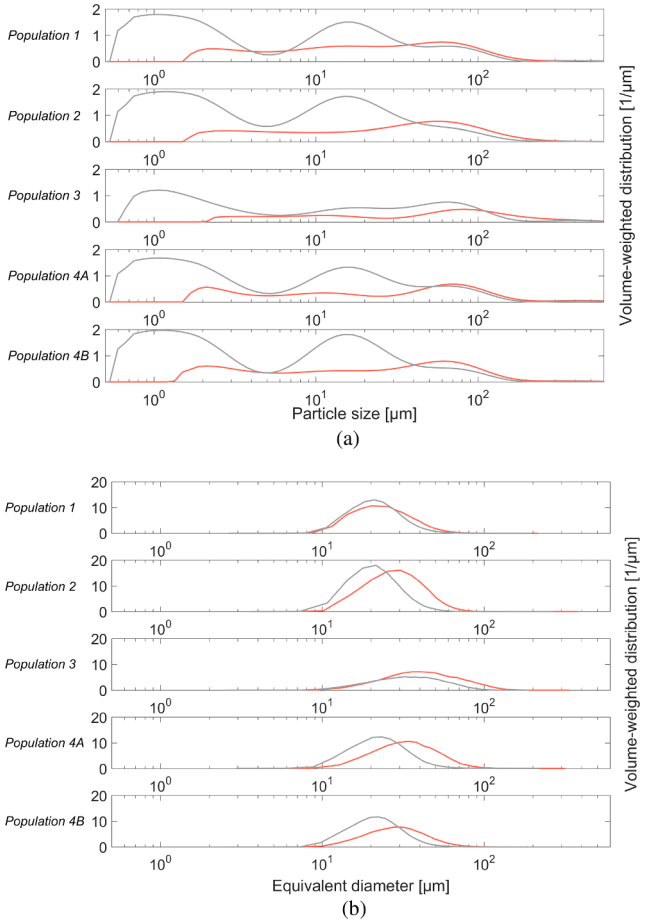

Fig. 4. (a) Volume-weighted PSDs of all populations presented in Table 1 resulting from LD measurements. LGA samples in red, MAN in gray. (b) Volume-weighted distributions of the equivalent diameters of all populations presented in Table 1. This characteristic size is calculated as the diameters of a sphere having the same volume of the needle particles (cylinders) characterized with PSSDs measurements. LGA samples in red, MAN in gray. (For interpretation of the references to color in this figure legend, the reader is referred to the web version of this article.)

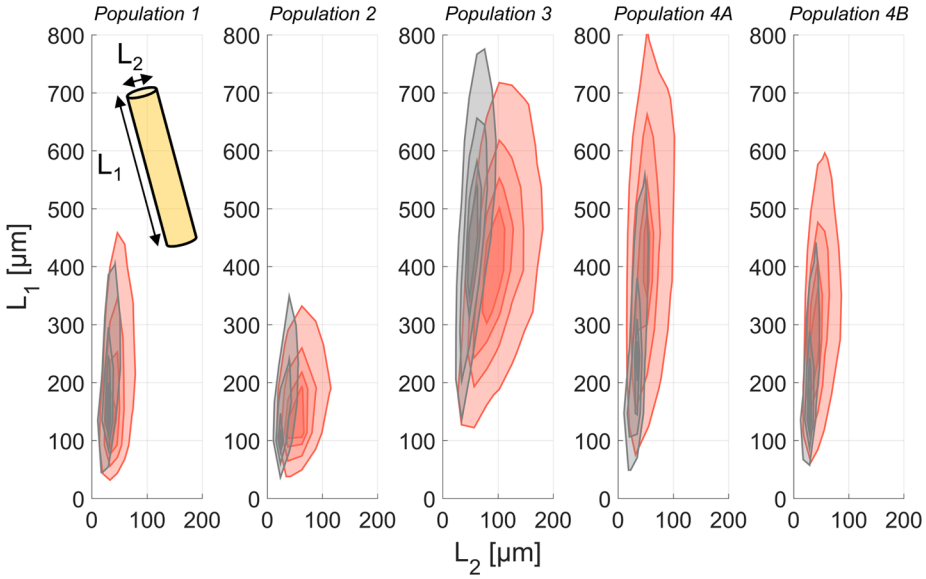

Fig. 5. Volume-weighted PSSDs of all populations presented in Table 1. LGA samples in red, MAN in gray. Contour lines were drawn at 20%, 50%, 75% and 90% of the maximum of each distribution. The yellow cylinder shown as inset in the population 1 PSSD illustrates the meaning of L_1 and L_2. (For interpretation of the references to color in this figure legend, the reader is referred to the web version of this article.)

first striking disagreement is the population range, which is a consequence of the technology behind the measurement techniques. The FTC relies on capturing images of the crystals with cameras, which limits the smallest detectable particle size to about 10 µm (limited by the resolution of the cameras and the optics, as well as by considerations regarding the field of view of the instrument). Conversely, the lower detection limit of laser diffraction measurements is in the submicron range. The second striking difference is apparent when comparing the size range that falls within the measurement window of the two instruments (i.e., larger particle sizes): the LD measurements are multi-modal in this range, while the FTC reports a unimodal distribution. A likely root cause for this is that the PSD reconstruction algorithm used in the LD instrument assumes that the scattering pattern stems from spherical particles; yet, in reality, it stems from rod-like particles [46]. The multiple modes detected in the LD measurements in the observable range of the FTC are therefore likely to be artifacts, as shown in the literature previously [35]. Apart from this, the FTC measurements obviously yield direct information about the shape of particles, while the LD measurements do not.

3.2. Filterability of crystals

The populations of crystals mentioned above were filtered under controlled conditions in order to determine the average specific cake resistance of consolidated cakes at different pressure drops. An overview of the results obtained for LGA (red) and MAN (gray) is presented in Fig. 6(a). In this figure the diameter of the symbols is proportional to the pressure drop. The results show that there are clear differences in filterability for the different populations and that there is a similar trend for the two compounds. Populations 2, which contain a large amount of fines and small particles, yield high cake resistances while populations 3 exhibit the best filtration performances, which is consistent with the fact that they contain larger crystals with lower aspect ratio. When comparing the results of different compounds with each other, the trends in filterabilities are similar, but the absolute values of cake resistances are about one order of magnitude higher for MAN. The effect of pressure drop on the filterability of stable cakes can also be observed from these results. The following observations can be made: first, a dependency of the cake resistance on pressure is apparent for

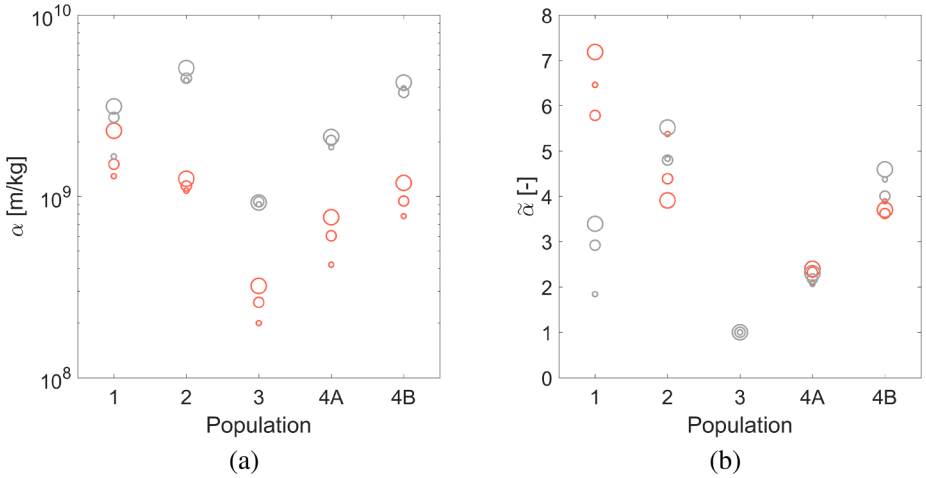

Fig. 6. Summary of resistances of filter cakes that reached a stable compaction after multiple percolations. The diameter of the circles scales linearly with the pressure drop that they represent: (a) absolute cake resistances, α; (b) relative cake resistances, $\tilde{\alpha}$.

both compounds, and second, the dependency is different from population to population. Eq. (5) predicts a linear dependency of the cake resistance on the pressure drop if there is no further compression/consolidation of the cake. To highlight that different populations of particles are compressing differently, in Fig. 6 we plot relative cake resistances (as defined in Eq. (6)). Therefore, by definition, populations whose behavior with increasing pressure matches the behavior of population 3 of each compound exhibit overlapping symbols in this figure. This is the case (at least roughly) for populations 3 (by definition), 4A and 4B of LGA and populations 3 (again, by definition) and 4A of MAN. All other populations exhibit a different compression behavior with increasing pressure drop. By using relative cake resistances in the modeling efforts that follow, we can therefore expect to remove some, but not all, of the effects of compressibility, of the properties of the solids and liquids, as well as their interactions.

3.3. Filterability prediction via regression analysis

In order to investigate the link between filtration performance and particle size and shape, we performed a regression analysis on the cake resistances obtained experimentally, using the outputs of particle characterization as predictors. Since absolute cake resistances are affected by pressure drop, surface properties of the particles, as well as properties of the mother liquor, we restrict ourselves to an analysis of relative cake resistances, $\tilde{\alpha}$ (cf. Eq. (6)).

3.3.1. Influence of predictor selection

The PLS regression was calibrated on the relative cake resistances of all populations measured at 1.50 barg (i.e., 5 datapoints) of either LGA or MAN; then the remaining 25 relative cake resistances, i.e., the same compound at 0.75 barg and 2.25 barg, as well as the other at 0.75 barg, 1.50 barg and 2.25 barg, are predicted. The mean absolute error between model and calibration data monotonically decreases when increasing the number of latent variables (LVs) in the PLS regression. However, selecting a high number of LVs might lead to overfitting, i.e., a model calibrated with a high number of LVs would only perform well on the calibration set, but could perform worse on data that it has not been calibrated with. This is avoided using the afore-mentioned cross-validation procedure.

The calibrated models (based on the 5 datapoints at 1.50 barg) were applied to the test cases (10 datapoints for the calibration substance, 15 datapoints for the other). In Figs. 7 and 8, we report the predicted

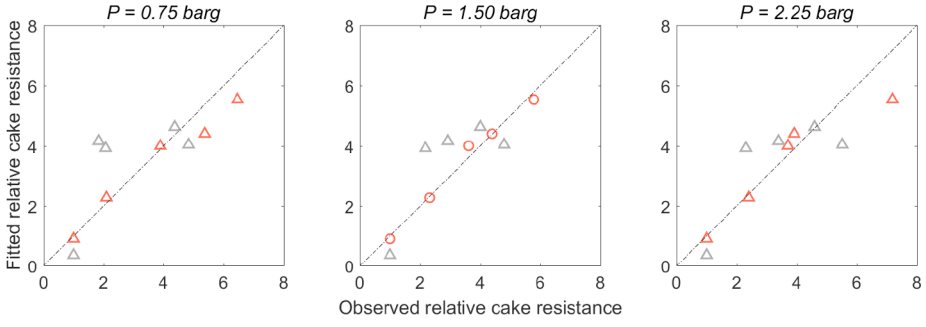

(a) Case 1

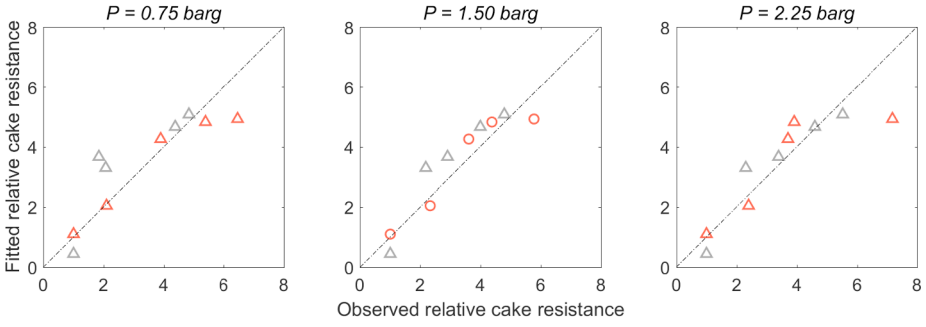

(b) Case 2

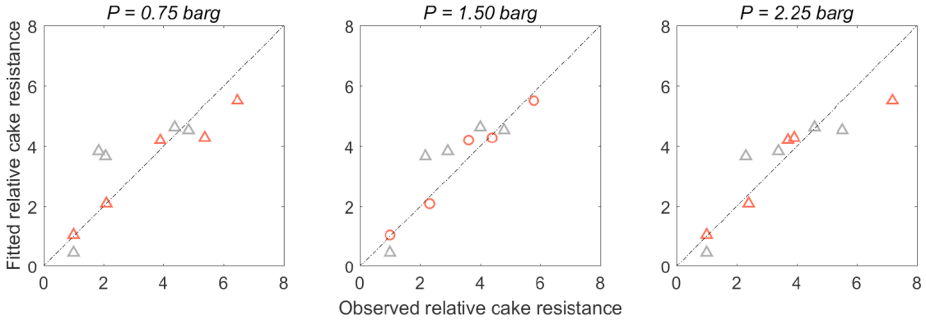

(c) Case 3

Fig. 7. Observed versus fitted cake resistance for three different regression types investigated. The data used for calibration are the experimental cake resistances obtained for the five populations of LGA at 1.50 barg. LGA results in red, MAN in gray. The data shown with circles are the calibration data, while predicted data are shown with triangles. (a) Case 1 – analysis based on the PSSD statistics; (b) case 2 – analysis based on the quantiles of the PSD distributions obtained with LD measurements; (c) case 3 – analysis done using the input data of both previous cases. (For interpretation of the references to color in this figure legend, the reader is referred to the web version of this article.)

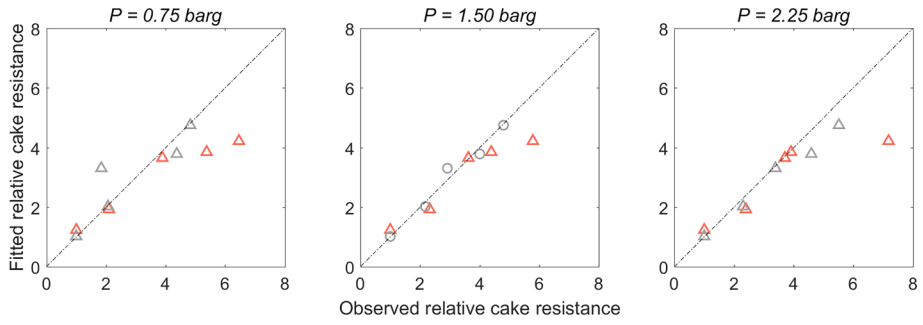

(a) Case 1

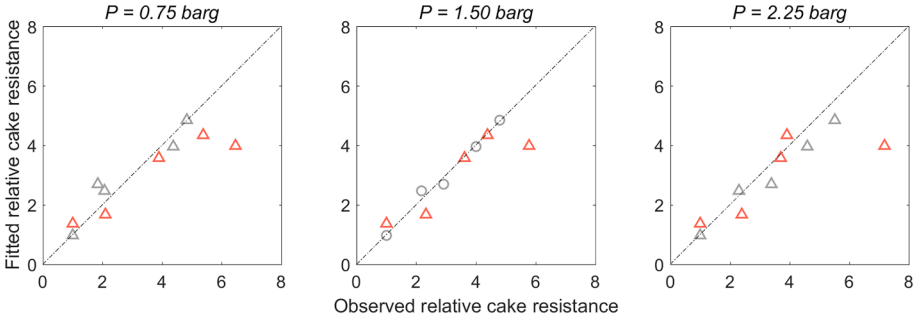

(b) Case 2

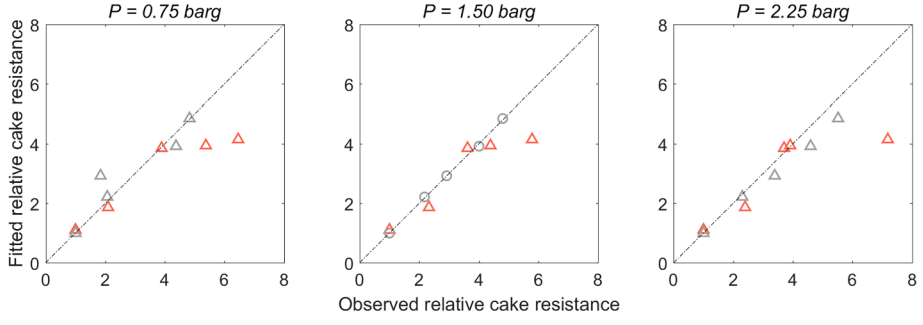

(c) Case 3

Fig. 8. Observed versus fitted cake resistance for three different regression types investigated. The data used for calibration are the experimental cake resistances obtained for the five populations of MAN at 1.50 barg. LGA results in red, MAN in gray. The data shown with circles are the calibration data, while predicted data are shown with triangles. (a) Case 1 – analysis based on the PSSD statistics; (b) case 2 – analysis based on the quantiles of the PSD distributions obtained with LD measurements; (c) case 3 – analysis done using the input data of both previous cases. (For interpretation of the references to color in this figure legend, the reader is referred to the web version of this article.)

relative cake resistances against the experimentally observed relative cake resistances for all data points and all model variants (LGA in red, MAN in gray); data points used for calibration purposes are shown as circles (LGA in Fig. 7 and MAN in Fig. 8), while predictions are plotted as triangles. The agreement between predicted and observed relative cake resistances is good for the datapoints used in the calibration, as expected (circles in the center panels). This visual impression is consistent with the MAEs reported in Tables 5 and 6 (calibration columns).

Focusing on the predicted data for the calibration compound (i.e., at pressures of 0.75 barg and 2.25 barg), all sets of descriptors yield an acceptable agreement between predicted and observed relative cake resistances (red points in the left and right panels in Fig. 7 and gray points in the left and right panels in Fig. 8), but the agreement is clearly worse than for the calibration set at 1.50 barg. The MAEs reported in Tables 5 and 6 (calibration compound predicted columns) are in agreement with this observation. Which set of descriptors performs best appears to be dependent on which compound is used for calibration.

Applying the PLS model calibrated on one substance to the other, the agreement between predicted and observed relative cake resistances is still acceptable (gray datapoints in Fig. 7; red points in Fig. 8). Considering the MAE values, we see that the PSD quantiles outperform the PSSD statistics when predicting MAN from LGA data or vice versa. This finding can be rationalized by considering the particle size distributions reported above: many fines were detected using LD in a particle size range too small to be measured with an image analysis method like the FTC. Since the amount of fines is very different between the two compounds, a calibration model based on one compound and descriptors that do not represent the amount of fines accurately (case 1) is likely to predict the other compound worse. However, combining the two sets of predictors (i.e., PSSD statistics and PSD quantiles, case 3),

Table 5
Summary of the mean absolute errors (MAE) for the calibration and test sets when LGA is used for calibration. The results for all the combinations of predictors are presented.

Case	LGA		MAN	All samples
	Calibration	Predicted	Predicted	
1	0.16	0.50	1.03	0.71
2	0.46	0.68	0.65	0.63
3	0.25	0.53	0.79	0.61

Table 6
Summary of the mean absolute errors (MAE) for the calibration and test sets when MAN is used for calibration. The results for all the combinations of predictors are presented.

Case	MAN		LGA	All samples
	Calibration	Predicted	Predicted	
1	0.16	0.41	0.73	0.53
2	0.13	0.39	0.83	0.57
3	0.04	0.36	0.72	0.49

we see that independently of the calibration compound the overall best result is obtained (see "All samples" columns in Tables 5 and 6).

Further insight on the comparison between the different cases can be gained by analyzing the importance of each variable used in the PLS models as characterized by VIP scores. These values enable us to infer what aspect of the descriptor data is important in order to correctly predict filterability. Fig. 9 displays the scores for the three different cases, comparing in each case the results for the model calibrated on LGA with those based on MAN. Evidently, the trends are significantly dependent on the calibration compound. It is particularly interesting to notice that in case 2 (PSD quantiles) moving towards the right of the graph for LGA the variables gradually show less importance, while for MAN the opposite occurs. Going in this direction we move towards larger quantiles, i.e., larger particle sizes. This shift in importance is potentially caused by the fact that LGA particle populations contain a significantly smaller amount of fines compared to MAN. This results in a higher number of quantiles relating to fine particles in the case of MAN compared to LGA hence in lower VIP scores for each of those quantiles individually. A further observation is that in case 1 the range of scores is broad, with variables showing noteworthy importance and others that appear to be irrelevant. These as well change depending on the substance used for calibration. Furthermore when the two sets of data are combined (case 3) their relative importance changes: the scores for the PSD quantiles shift to higher values, while the PSSD statistics generally shift downward.

3.4. Sensitivity to training strategy

The results shown before highlight the strong dependency of the predictive performance of the regression analysis on the calibration technique adopted. We therefore present here an analysis of the sensitivity on the number and type of calibration points for one of the cases investigated above, namely case 3 where both PSD quantiles and PSSD statistics are used as descriptors of the crystals. To this end, we selected all possible combinations of 2, 3, 4 and 5 datapoints at 1.50 barg as calibration sets and generated a PLS model for each selection. We then evaluated the predictive capability of each such PLS model based on the MAEs of the remaining samples of the calibration compound, as well as of the other compound. The aim is to understand if there is a particular set of data points that would improve the performance of the model and if it is possible to identify a pattern to infer what type of points should be considered for calibration and how many.

The results are summarized in Fig. 10. In Fig. 10(a) each point represents the outcome of a PLS regression using different sets of LGA data for calibration. The points in the subfigure on the left indicate the MAE of the predicted points of LGA for each number of calibration points. The subfigure on the right, analogously indicates the MAEs for MAN, which is here the fully predicted compound. Fig. 10(b), similarly, presents the error metrics that can be obtained if MAN is used as the calibration compound. Increasing the number of calibration points the variability of results decreases, reducing the probability of having calibration data that poorly represents the overall set. The lowest MAE for a given number of calibration points of the purely predicted compound is always higher than the one of the calibration substance. Moreover, we notice that the best calibration strategy is not the one with the total data set. This indicates that some of the additional calibration data add noise rather than useful information, thus making the model less accurate.

Looking however at which combination gives the best condition, no specific pattern can be detected, as can be seen from the values given in the supplementary material. Comparing the results arising from calibrating on different compounds, it can be seen that when MAN is selected the difference, in terms of lowest MAEs, between MAN and LGA becomes smaller.

How well each model variant predicts the ranking of filterabilities can be analyzed using Kendall's τ. To this end, for each calibration strategy the predicted rank of the responses is estimated for the

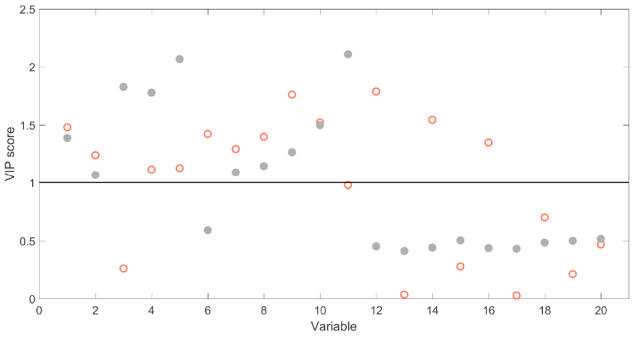

(a) Case 1

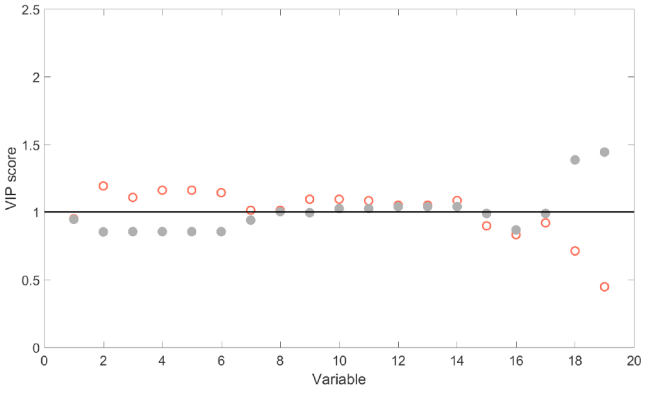

(b) Case 2

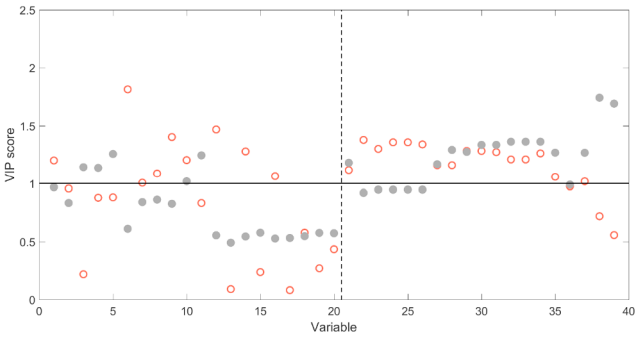

(c) Case 3

Fig. 9. VIP scores for the calibration variables based on 5 calibration points of LGA (red empty symbols), and MAN (gray filled points). (a) Case 1 – analysis based on the PSSD statistics; (b) case 2 – analysis based on the quantiles of the PSD distributions obtained with LD measurements; (c) case 3 – analysis done using the input data of both previous cases. (For interpretation of the references to color in this figure legend, the reader is referred to the web version of this article.)

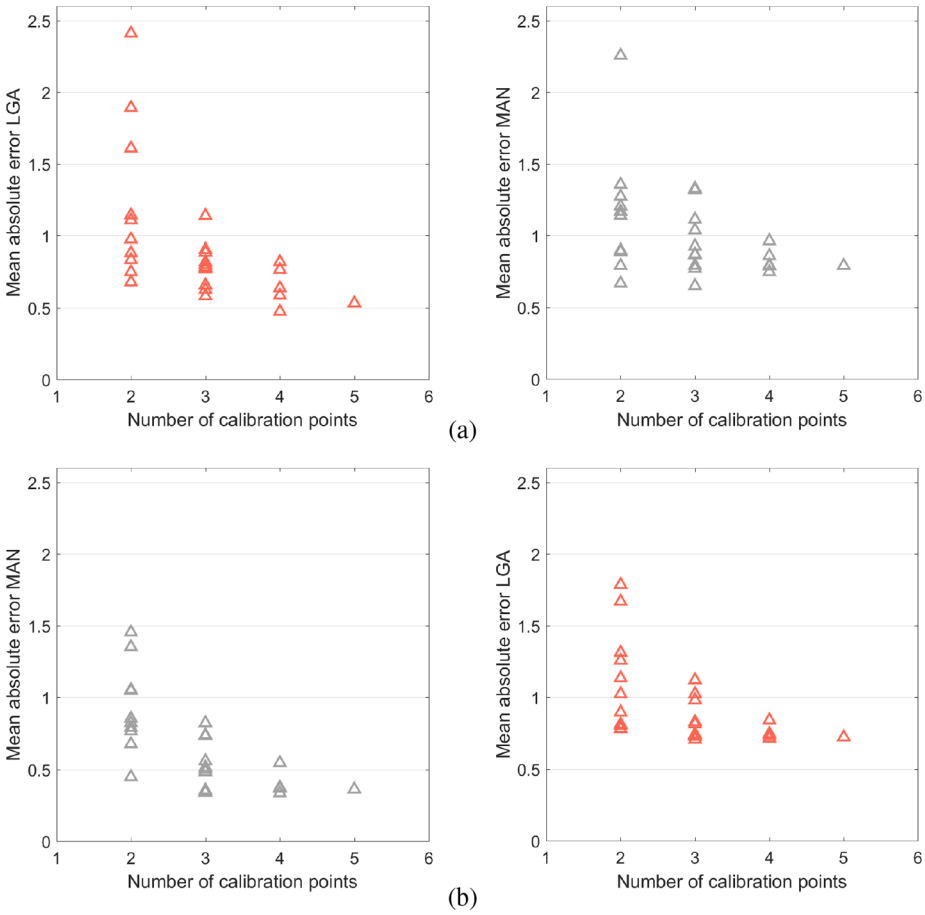

Fig. 10. Mean absolute errors (MAE) for the predicted points of the calibration compound (on the left) and the purely forecasted one (on the right). These PLS models (case 3) use all possible combinations of calibration points at P = 1.50 barg: (a) calibration on LGA; (b) calibration on MAN.

calibration compound and the purely predicted one. These are then compared to the measured ones and the degree of accordance is expressed in terms of τ. Fig. 11 illustrates the outcome of this evaluation, showing on the left the results for the calibration substance and on the right those for the predicted compound. Symbols with a diameter that scales linearly with pressure drop are used to show all the possible cases. Visibly, the range of results obtained decreases with an increasing number of calibration points converging towards virtually perfect matching. This is the case for the calibration pressure (mid-sized symbols) but also for the predicted pressures. It is worth pointing out that a datapoint of MAN at 0.75 barg seems to recurrently cause a deviation between measured and expected results. This is clearly highlighted from the ranking outcome of the models calibrated with 5 points from MAN. This hints at the fact that this point could be an outlier. Apart from this point, this analysis indicates that selecting all five calibration points of one compound at a single pressure allows to correctly predict the filterability ranking for both compounds at all pressures. This is the case even if the underlying PLS models do not have the lowest MAEs.

4. Concluding remarks and recommendations

In this work the link between particle size and shape and filterability was analyzed with a PLS regression correlating relative cake resistances with properties of particle size (and shape) distributions for two compounds that exhibit needle-like crystal morphologies, β L-Glutamic Acid and γ D-Mannitol. The 1D particle size distribution and the nD particle size and shape distributions were obtained using laser diffraction, a routine characterization technique, and the flow through cell, a custom-built stereoscopic imaging system, respectively. While the FTC rigorously measures the size and shape of needle-like particles above its detection limit, it fails to characterize fines accurately. Conversely, the LD method erroneously reports size distributions with multiple modes when measuring rod-like particles. Nevertheless, it is able to detect fine particles very well.

Our PLS regression results show that both types of data have their merits. For D-Mannitol large amounts of fines are present in some particle populations, which makes detecting them paramount. Therefore, PLS regressions for D-Mannitol based on LD data tend to outperform regressions based on FTC data. For L-Glutamic Acid on the other hand, there are fewer fines present and the amount of fines is comparable between different populations, so that a differentiation of different shapes becomes decisive to distinguish between the filterability of different populations. Hence, PSSD data generally performs better than LD data on L-Glutamic Acid samples. We also show that the combination of LD and FTC data gives the best predictability on the overall dataset. Having access to this wealth of data is therefore desirable; especially when transferring a PLS model calibrated on one compound to another. However, based on our analysis, it appears that for systems of needle-like crystals like those studied here the ability to correctly characterize fines is arguably more important than getting full shape information. However, this consideration might not be valid when moving to different shape domains.

While the quantitative predictions of relative cake resistances are satisfactory for a PLS regression based on combined LD and PSSD data, we have also shown that such a model is able to rank the relative cake resistances with near perfect agreement to experimentally obtained values. If one's goal is to qualitatively establish whether a given change

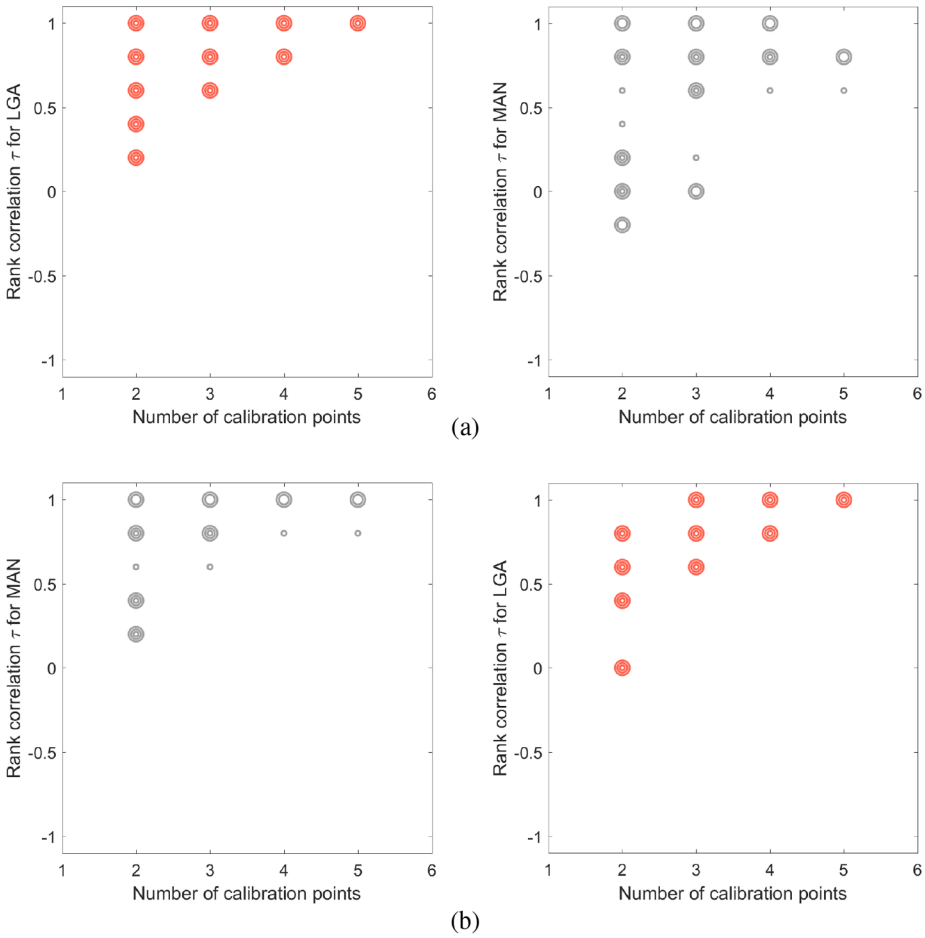

Fig. 11. Kendall's τ coefficient for the calibration compound (on the left) and the purely forecasted one (on the right). These PLS models (case 3) use all possible combinations of calibration points at P = 1.50 barg. The accordance at different pressures is expressed with symbols of different size. The diameter of the circles scales linearly with the pressure drop: (a) calibration on LGA; (b) calibration on MAN.

in the PSD or PSSD will be beneficial in terms of filtration performance, i.e., without predicting the magnitude of the improvement, knowing the ranking is sufficient and our approach delivers it with high confidence.

In terms of assessing the impact of relatively simple operations to change the filterability of crystals, e.g., milling followed by a single temperature cycle, our study shows that such operations have led to a substantial improvement of filtration performance in comparison to crystals produced in a simple batch cooling crystallization. This is evidenced by the roughly 3 and 6 times lower cake resistance measured for population 3 in comparison to population 1 for D-Mannitol and L-Glutamic Acid, respectively. Naturally, this would be economically beneficial as long as the gain obtained in filtration is higher than the burden caused by the shape/size manipulation step.

The use of the approach presented here therefore allows predicting the relative cake resistance of further needle-like crystals with comparable PS(S)Ds. to the compounds studied. The knowledge of the relative cake resistance enables us to predict which batch from a given series filters best based solely on shape and size information. Therefore, our approach—when further developed—should allow to predict which crystallization procedure will result in the most filterable suspension.

Acknowledgements

TV thanks the Royal Academy of Engineering for support through an Engineering for Development research fellowship. GP and TV thank AstraZeneca and EPSRC for the iCASE award (voucher number 16000111) supporting GP's PhD project.

Appendix A. Supplementary material

Supplementary data associated with this article can be found, in the online version, at https://doi.org/10.1016/j.seppur.2018.10.042.

References

[1] C. Wibowo, W.C. Chang, K.M. Ng, Design of integrated crystallization systems, AIChE J. 47 (11) (2001) 2474–2492, https://doi.org/10.1002/aic.690471111.
[2] R. Wakeman, S. Tarleton, Solid/liquid Separation: Principles of Industrial Filtration, Elsevier, 2005.
[3] A. Jones, J. Budz, J. Mullin, Batch crystallization and solid-liquid separation of potassium sulphate, Chem. Eng. Sci. 42 (4) (1987) 619–629, https://doi.org/10.1016/0009-2509(87)80023-4.
[4] R. Beck, A. Häkkinen, D. Malthe-Sørenssen, J.-P. Andreassen, The effect of crystallization conditions, crystal morphology and size on pressure filtration of l-glutamic acid and an aromatic amine, Sep. Purif. Technol. 66 (3) (2009) 549–558, https://doi.org/10.1016/j.seppur.2009.01.018.
[5] A. Häkkinen, K. Pöllänen, M. Karjalainen, J. Rantanen, M. Louhi-Kultanen, L. Nyström, Batch cooling crystallization and pressure filtration of sulphathiazole: the influence of solvent composition, Biotechnol. Appl. Biochem. 41 (Pt 1) (2005) 17–28, https://doi.org/10.1042/BA20040044.
[6] A. Häkkinen, K. Pöllänen, S.-P. Reinikainen, M. Louhi-Kultanen, L. Nyström, Prediction of filtration characteristics by multivariate data analysis, Filtration 8 (2) (2008) 144–153.
[7] A. Häkkinen, The Influence of Crystallization Conditions on the Filtration Characteristics of Sulphathiazole (Ph.D. thesis), Lappeenranta University of Technology, Finland, 2009.
[8] R. Wakeman, The influence of particle properties on filtration, Sep. Purif. Technol. 58 (2) (2007) 234–241, https://doi.org/10.1016/j.seppur.2007.03.018.
[9] J. Kozeny, Über kapillare Leitung des Wassers im Boden, Sitzungsber Akad. Wiss., Wien 136 (2a) (1927) 271–306.
[10] P.C. Carman, Fluid flow through granular beds, Chem. Eng. Res. Des. 75 (1997) S32–S48, https://doi.org/10.1016/S0263-8762(97)80003-2.

[11] D. Bourcier, J.P. Féraud, D. Colson, K. Mandrick, D. Ode, E. Brackx, F. Puel, Influence of particle size and shape properties on cake resistance and compressibility during pressure filtration, Chem. Eng. Sci. 144 (2016) 176–187, https://doi.org/10.1016/j.ces.2016.01.023.
[12] M. Fujiwara, Z.K. Nagy, J.W. Chew, R.D. Braatz, First-principles and direct design approaches for the control of pharmaceutical crystallization, J. Process Control 15 (5) (2005) 493–504, https://doi.org/10.1016/j.jprocont.2004.08.003.
[13] M.A. Lovette, A.R. Browning, D.W. Griffin, J.P. Sizemore, R.C. Snyder, M.F. Doherty, Crystal shape engineering, Ind. Eng. Chem. Res. 47 (24) (2008) 9812–9833, https://doi.org/10.1021/ie800900f.
[14] T. Vetter, C.L. Burcham, M.F. Doherty, Regions of attainable particle sizes in continuous and batch crystallization processes, Chem. Eng. Sci. 106 (2014) 167–180, https://doi.org/10.1016/j.ces.2013.11.008.
[15] F. Salvatori, M. Mazzotti, Manipulation of particle morphology by crystallization, milling, and heating cycles—a mathematical modeling approach, Ind. Eng. Chem. Res. 56 (32) (2017) 9188–9201, https://doi.org/10.1021/acs.iecr.7b02070.
[16] S. Schorsch, D. Ochsenbein, T. Vetter, M. Morari, M. Mazzotti, High accuracy online measurement of multidimensional particle size distributions during crystallization, Chem. Eng. Sci. 105 (2014) 155–168.
[17] C. Borchert, E. Temmel, H. Eisenschmidt, H. Lorenz, A. Seidel-Morgenstern, K. Sundmacher, Image-based in situ identification of face specific crystal growth rates from crystal populations, Cryst. Growth Des. 14 (3) (2014) 952–971, https://doi.org/10.1021/cg401098x.
[18] S. Schorsch, J.-H. Hours, T. Vetter, M. Mazzotti, C.N. Jones, An optimization-based approach to extract faceted crystal shapes from stereoscopic images, Comput. Chem. Eng. 75 (2015) 171–183, https://doi.org/10.1016/j.compchemeng.2015.01.016.
[19] A.K. Rajagopalan, J. Schneeberger, F. Salvatori, S. Bötschi, D.R. Ochsenbein, M.R. Oswald, M. Pollefeys, M. Mazzotti, A comprehensive shape analysis pipeline for stereoscopic measurements of particulate populations in suspension, Powder Technol. 321 (2017) 479–493, https://doi.org/10.1016/j.powtec.2017.08.044.
[20] Z.H. Loh, A.K. Samanta, P.W. Sia Heng, Overview of milling techniques for improving the solubility of poorly water-soluble drugs, Asian J. Pharm. Sci. 10 (4) (2014) 255–274, https://doi.org/10.1016/j.ajps.2014.12.006.
[21] M. Lovette, M. Muratore, M.F. Doherty, Crystal shape modification through cycles of dissolution and growth: attainable regions and experimental validation, AIChE J. 58 (2012) 1465–1474.
[22] R.C. Snyder, S. Studener, M.F. Doherty, Manipulation of crystal shape by cycles of growth and dissolution, AIChE J. 53 (6) (2007) 1510–1517, https://doi.org/10.1002/aic.11174.
[23] M.R. Abu Bakar, Z.K. Nagy, C.D. Rielly, Investigation of the effect of temperature cycling on surface features of sulfathiazole crystals during seeded batch cooling crystallization, Cryst. Growth Des. 10 (9) (2010) 3892–3900, https://doi.org/10.1021/cg1002379.
[24] R. Beck, K. Svinning, A. Häkkinen, D. Malthe-Sørenssen, J.P. Andreassen, Analysis of filtration characteristics for compressible polycrystalline particles by partial least squares regression, Sep. Sci. Technol. 45 (9) (2010) 1196–1208, https://doi.org/10.1080/01496391003705649.
[25] D.R. Ochsenbein, S. Schorsch, T. Vetter, M. Mazzotti, M. Morari, Growth rate estimation of β L-glutamic acid from online measurements of multidimensional particle size distributions and concentration, Ind. Eng. Chem. Res. 53 (2014) 9136–9148.
[26] R. Ho, M. Naderi, J.Y.Y. Heng, D.R. Williams, F. Thielmann, P. Bouza, A.R. Keith, G. Thiele, D.J. Burnett, Effect of milling on particle shape and surface energy heterogeneity of needle-Shaped crystals, Pharm. Res. 29 (10) (2012) 2806–2816, https://doi.org/10.1007/s11095-012-0842-1.
[27] C.V. Luciani, E.W. Conder, K.D. Seibert, Modeling-aided scale-up of high-shear rotor-stator wet milling for pharmaceutical applications, Org. Process Res. Dev. 19 (5) (2015) 582–589, https://doi.org/10.1021/acs.oprd.5b00066.
[28] M.R. Bakar, Z.K. Nagy, C.D. Rielly, Seeded batch cooling crystallization with temperature cycling for the control of size uniformity and polymorphic purity of sulfathiazole crystals, Org. Process Res. Dev. 13 (6) (2009) 1343–1356, https://doi.org/10.1021/op900174b.
[29] G.A. Bunin, F.V. Lima, C. Georgakis, C.M. Hunt, Model predictive control and dynamic operability studies in a stirred tank: rapid temperature cycling for crystallization, Chem. Eng. Commun. 197 (5) (2010) 733–752, https://doi.org/10.1080/00986440903288096.
[30] E. Simone, A.R. Klapwijk, C.C. Wilson, Z.K. Nagy, Investigation of the evolution of crystal size and shape during temperature cycling and in the presence of a polymeric additive using combined process analytical technologies, Cryst. Growth Des. 17 (4) (2017) 1695–1706, https://doi.org/10.1021/acs.cgd.6b01683.
[31] H. Eisenschmidt, N. Bajcinca, K. Sundmacher, Optimal control of crystal shapes in batch crystallization experiments by growth-dissolution cycles, Cryst. Growth Des. 16 (6) (2016) 3297–3306, https://doi.org/10.1021/acs.cgd.6b00288.
[32] G. Eshel, G.J. Levy, U. Mingelgrin, M.J. Singer, Critical evaluation of the use of laser diffraction for particle-size distribution analysis, Soil Sci. Soc. Am. J. 68 (3) (2004) 736–743, https://doi.org/10.2136/sssaj2004.7360.
[33] N. Stevens, J. Shrimpton, M. Palmer, D. Prime, B. Johal, Accuracy assessments for laser diffraction measurements of pharmaceutical lactose, Meas. Sci. Technol. 18 (12) (2007) 3697–3706, https://doi.org/10.1088/0957-0233/18/12/004.
[34] A.P. Tinke, A. Carnicer, R. Govoreanu, G. Scheltjens, L. Lauwerysen, N. Mertens, K. Vanhoutte, M.E. Brewster, Particle shape and orientation in laser diffraction and static image analysis size distribution analysis of micrometer sized rectangular particles, Powder Technol. 186 (2) (2008) 154–167, https://doi.org/10.1016/j.powtec.2007.11.017.
[35] O.S. Agimelen, A.J. Mulholland, J. Sefcik, Modelling of artefacts in estimations of particle size of needle-like particles from laser diffraction measurements, Chem. Eng. Sci. 158 (July 2016) (2017) 445–452, https://doi.org/10.1016/j.ces.2016.10.031 Available from: < arXiv:1603.03455 > .
[36] S. Schorsch, T. Vetter, M. Mazzotti, Measuring multidimensional particle size distributions during crystallization, Chem. Eng. Sci. 77 (2012) 130–142.
[37] H. Darcy, Les fontaines publiques de la ville de Dijon: exposition et application des principes à suivre et des formules à employer dans les questions de distribution d'eau, Recherche (1856) 647, https://doi.org/10.2516/ogst.
[38] S. Ripperger, W. Gösele, C. Alt, T. Loewe, Filtration, 1. Fundamentals, Ullmann's Encyclopedia of Industrial Chemistry, Wiley-VCH Verlag GmbH & Co. KGaA, 2000, pp. 25.1–25.40, , https://doi.org/10.1002/14356007.b02 (Ch. Filtration).
[39] S.-k. Teoh, R.B. Tan, C. Tien, A new procedure for determining specific filter cake resistance from filtration data, Chem. Eng. Sci. 61 (15) (2006) 4957–4965, https://doi.org/10.1016/j.ces.2006.03.048.
[40] C. Tien, Introduction to Cake Filtration: Analyses, Experiments and Applications, Chemical, Petrochemical & Process, Elsevier, 2006.
[41] P. Geladi, B.R. Kowalski, Partial least-squares regression: a tutorial, Anal. Chim. Acta 185 (C) (1986) 1–17, https://doi.org/10.1016/0003-2670(86)80028-9 Available from: < arXiv:1011.1669v > .
[42] MATLAB, Statistics and Machine Learning Toolbox ¢ User' s Guide R 2016 a, The MathWorks Inc., Natick, Massachusetts, 2016.
[43] S. Tie Jong, SIMPLS: an alternative approach squares regression to partial least, Elsevier Sci. Publ. B.V 18 (1993) 2–263, https://doi.org/10.1016/0169-7439(93)85002-X.
[44] I.G. Chong, C.H. Jun, Performance of some variable selection methods when multicollinearity is present, Chemometr. Intell. Lab. Syst. 78 (1) (2005) 103–112, https://doi.org/10.1016/j.chemolab.2004.12.011.
[45] M.G. Kendall, Rank Correlation Methods vol. 3, Oxford University Press, 1990.
[46] I. de Albuquerque, M. Mazzotti, D.R. Ochsenbein, M. Morari, Effect of needle-like crystal shape on measured particle size distributions, AIChE J. 62 (9) (2016) 2974–2985, https://doi.org/10.1002/aic.15270.